2023 DZ2 Planetary Defense Campaign

Vishnu Reddy, Michael S. Kelley, Lance Benner, Jessie Dotson, Nicolas Erasmus, Davide Farnocchia, Tyler Linder, Joseph R. Masiero, Cristina Thomas, James Bauer, et al.

The Planetary Science Journal, 5:141 (16pp), 2024 June https://doi.org/10.3847/PSJ/ad4a6d

2023 DZ2 Planetary Defense Campaign

Vishnu Reddy[1], Michael S. Kelley[2], Lance Benner[3], Jessie Dotson[4], Nicolas Erasmus[5], Davide Farnocchia[3], Tyler Linder[6], Joseph R. Masiero[7], Cristina Thomas[8], James Bauer[9], Miguel R. Alarcon[10,11], Paolo Bacci[12,13,14], Daniel Bamberger[15], Adam Battle[1], Zouhair Benkhaldoun[16], Guido Betti[17,18], Mirel Birlan[19,20], Marina Brozovic[3], Brian Burt[21], David C. Cantillo[1], Sunil Chandra[5], Gregoire Chomette[22], Ashley Coates[4], Francesca DeMeo[23], Maxime Devogèle[24], Petr Fatka[25], Marin Ferrais[23], Paolo Fini[16], Carel van Gend[5], Jon D. Giorgini[3], Dmitry Glamazda[26], Robert Holmes[6], Joseph L. Hora[27], Shinji Horiuchi[28], Kamil Hornoch[24], Marco Iozzi[13,29,30,31], Cristóvão Jacques[32,33], Emmanuel Jehin[34], Hai Jiang[35], Galina Kaiser[25], Peter Kušnirák[24], Eduard Kuznetsov[25], Julia de León[9,10], Alexios Liakos[36], Javier Licandro[9,10], Tim Lister[37], Jing Liu[34], Andy Lopez-Oquendo[8], Martina Maestripieri[11,12,13], Donovan Mathias[4], Marco Micheli[37,38], Shantanu P. Naidu[3], Alessandro Nastasi[39,40], Alin Nedelcu[18,19], Elisabeta Petrescu[33,37,38], Marcel Popescu[17], Stephen B. Potter[5], Petr Pravec[24], Juan Sanchez[41], Toni Santana-Ros[42,43], Miquel Serra-Ricart[9,10], Nick Sioulas[44], Adrian Sonka[18], Alessio Squilloni[13,29,30], Maura Tombelli[13,29,30], Madalina Trelia[18], David E. Trilling[8], Elizabeth Warner[9], Guy Wells[14], Lorien Wheeler[4], and Mike Wiles[45]

[1] Lunar and Planetary Laboratory, University of Arizona, Tucson, AZ 85721, USA; vishnureddy@arizona.edu
[2] Planetary Defense Coordination Office, Planetary Science Division, NASA Headquarters, Washington, DC 20546, USA
[3] Jet Propulsion Laboratory, California Institute of Technology, Pasadena, CA 91109, USA
[4] NASA Ames Research Center, Moffett Field, CA 94035, USA
[5] South African Astronomical Observatory, Cape Town, 7925, South Africa
[6] Astronomical Research Institute, 7168 NCR 2750E, Ashmore, IL 61912, USA
[7] Caltech/IPAC, 1200 East California Boulevard, MC 100-22, Pasadena, CA 91125, USA
[8] Northern Arizona University, Department of Astronomy and Planetary Science, Flagstaff, AZ 86011, USA
[9] University of Maryland, College Park, MD 20742, USA
[10] Instituto de Astrofísica de Canarias, C/Vía Láctea s/n, E-38205 La Laguna, Canarias, Spain
[11] Departamento de Astrofísica, Universidad de La Laguna, E-38205 La Laguna, Canarias, Spain
[12] Osservatorio Astronomico Montagna Pistoiese, San Marcello Piteglic (PT), Casella Postale 46, Italy
[13] GAMP Gruppo Astrofili Montagna Pistoiese, Italy
[14] UAI—Unione Astrofili Italiani, Padova, Italy
[15] Northolt Branch Observatories, Dabbs Hill Lane, Northolt, London, UK
[16] High Energy Physics and Astrophysics Laboratory, Cadi Ayyad University, Marrakech, Morocco
[17] Blessed Hermann Observatory, Florence, Italy
[18] SAF—Società Astronomica Fiorentina, 50019 Sesto Fiorentino FI, Italy
[19] Astronomical Institute of the Romanian Academy, 5 Cutitul de Argint, 040557 Bucharest, Romania
[20] IMCCE. Observatoire de Paris, France
[21] Lowell Observatory, 1400 West Mars Hill Road, Flagstaff, AZ 86001, USA
[22] STC at NASA Ames Research Center, Moffett Field, CA 94035, USA
[23] Massachusetts Institute of Technology, 77 Massachusetts Avenue, Cambridge, MA 02139, USA
[24] Arecibo Observatory, University of Central Florida, HC-3 Box 53995, Arecibo, PR 00612, USA
[25] Astronomical Institute AS CR, Fričova 298, Ondřejov, CZ-25165, Czech Republic
[26] Ural Federal University, Mira Street 19, Yekaterinburg, 620002, Russia
[27] Center for Astrophysics, Harvard & Smithsonian, 60 Garden Street, MS-65, Cambridge, MA 02138, USA
[28] Canberra Deep Space Communication Complex, CSIRO, Tidbinbilla, Australia
[29] H.O.B. Astronomical Observatory, Capraia FI, Italy
[30] GRAM Gruppo Astrofili Montelupo, Montelupo fiorentino FI, Italy
[31] Osservatorio Astronomico "Beppe Forti," Montelupo fiorentino FI, Italy
[32] SONEAR Observatory, Morro do Diamante, Oliveira, Minas Gerais, Brazil
[33] CEAMIG (Centro de Estudos Astronomicos de Minas Gerais) Rua dos Aimores, 2735 Belo Horizonte, Barro Preto Minas Gerais, Brazil
[34] Space Sciences, Technologies & Astrophysics Research (STAR) Institute, University of Liège, Allée du 6 Août 19, 4000 Liège, Belgium
[35] National Astronomical Observatories, Chinese Academy of Sciences, 20A Datun Road, Chaoyang District, Beijing, People's Republic of China
[36] Institute for Astronomy, Astrophysics, Space Applications and Remote Sensing (IAASARS), National Observatory of Athens, Metaxa & Vas. Pavlou St., GR-15773, Penteli, Athens, Greece
[37] Las Cumbres Observatory (LCOGT), 6740 Cortona Drive, Suite 102, Goleta, CA 93117, USA
[38] ESA NEO Coordination Centre, Largo Galileo Galilei, 1, I-00044 Frascati (RM), Italy
[39] GAL Hassin—Centro Internazionale per le Scienze Astronomiche. Via della Fontana Mitri 3, 90010 Isnello, Palermo, Italy
[40] INAF—Osservatorio Astronomico di Palermo, Piazza del Parlamento, 1, 90134 Palermo, Italy
[41] Planetary Science Institute, Tucson, AZ, USA
[42] Departamento de Física, Ingeniería de Sistemas y Teoría de la Señal, Universidad de Alicante, Carr. de San Vicente del Raspeig, s/n, 03690 San Vicente del Raspeig, Alicante, Spain
[43] Institut de Ciències del Cosmos (ICCUB), Universitat de Barcelona (IEEC-UB), Carrer de Martí i Franquès, 1, 08028, Barcelona, Spain
[44] NOAK Observatory, Delfon 2 Stavraki, Ioannina, 45500, Greece
[45] NAC Observatory, Benson, AZ, USA

Received 2024 February 21; revised 2024 May 8; accepted 2024 May 9; published 2024 June 13

Abstract

We present the results of a fourth planetary defense exercise, focused this time on the small near-Earth asteroid (NEA) 2023 DZ2 and conducted during its close approach to the Earth in 2023 March. The International Asteroid Warning Network (IAWN), with support from NASA's Planetary Defense Coordination Office (PDCO), has been coordinating planetary defense observational campaigns since 2017 to test the operational readiness of the global planetary defense capabilities. The last campaign focused on the NEA Apophis, and an outcome of that exercise was the need for a short burst campaign to replicate a real-life near-Earth object impact hazard scenario. The goal of the 2023 DZ2 campaign was to characterize the small NEA as a potential impactor and exercise the planetary defense system including observations, hypothetical risk assessment and risk prediction, and hazard communication with a short notice of just 24 hr. The entire campaign lasted about 10 days. The campaign team was divided into several working groups based on the characterization method: photometry, spectroscopy, thermal IR photometry and optical polarimetry, radar, and risk assessment. Science results from the campaign show that 2023 DZ2 has a rotation period of 6.2745 ± 0.0030 minutes; visible wavelength color photometry/spectroscopy/polarimetry and near-IR spectroscopy all point to an E-type taxonomic classification with surface composition analogous to aubrite meteorites; and radar observations show that the object has a diameter of 30 ± 10 m, consistent with the high albedo (0.49) derived from polarimetric and thermal IR observations.

Unified Astronomy Thesaurus concepts: Asteroids (72); Achondrites (15); Near-Earth objects (1092); Small Solar System bodies (1469); Close encounters (255)

1. Introduction

Impacts due to near-Earth objects (NEOs) have shaped the course of life on Earth. Evidence for this is present in the form of mass extinction events, impact craters, and witnessed bolide events such as the 2013 Chelyabinsk event. Detecting these hazards ahead of time is the first step in the mitigation strategy. NASA established the Planetary Defense Coordination Office to coordinate planetary defense efforts in the United States. The United Nations established the International Asteroid Warning Network in 2013 to coordinate international efforts between organizations involved in detecting, tracking, and characterizing NEOs. IAWN is also tasked with developing a communication plan to assist governments in the analysis of asteroid impact consequences and the planning of mitigation responses. So far, we have conducted three planetary defense campaigns (Reddy et al. 2019, 2022a, 2022b) to test the global planetary defense operational readiness.

These three earlier campaigns were based on targets known with ample lead time to be headed for a close flyby of the Earth with sufficient notice, which enabled us to plan and execute these campaigns over the course of several months. An action item stemming from the last campaign focused on Apophis (Reddy et al. 2022b) was that a future campaign should focus on rapid characterization of an NEO to better simulate a real-world scenario with a shorter, more realistic advance notice. To address this potential situation, on 2023 March 19, we launched a rapid response characterization campaign focused on the newly discovered NEO 2023 DZ2 with less than 24 hr notice. The Minor Planet Center (MPC) announced the discovery of 2023 DZ2 on 2023 March 16.[46] The object was discovered by the EURONEAR project using the Isaac Newton Telescope (MPC Code 950). The object was headed for a close approach to Earth within 0.45 lunar distances (0.0117 au) on 2023 March 25. Given its initial absolute magnitude $H = 23.5$, the expected size was 50–110 m. Data collection for this campaign started on March 20 at 13:00 UTC.

Here, we present results from each of the working groups from the 2023 DZ2 campaign. The goals of the campaign were to determine operationally relevant science products in a timely manner that can be used for hazard modeling. The 2023 DZ2 campaign followed protocols that were refined based on experience from the three previous exercises. Campaign participation was voluntary, with nearly 50 participants from over 15 nations. Participants were organized into six working groups: Astrometry, Photometry, Spectroscopy, Radar, Thermal Modeling/Polarimetry, and Hazard Modeling.

2. Discovery and Close Approach

Near-Earth asteroid 2023 DZ2 was discovered by La Palma (observatory code 950) on 2023 February 27 at a solar elongation of 140° and apparent magnitude $V = 21$ (Popescu et al. 2023; MPEC 2023-F12). 2023 DZ2 is an Apollo asteroid with an orbit nearly tangent to that of the Earth, as shown in Figure 1. The perihelion distance is 0.99 au, the semimajor axis is 2.16 au, the eccentricity is 0.54, the orbital period is 3.2 yr, and the inclination is nearly zero.[47]

Upon discovery, it became clear that the asteroid was headed for a close approach with Earth on 2023 March 25 at a geocentric distance of 175,000 km (about 0.45 lunar distances). 2023 DZ2 approached Earth from the northern sky and with an inbound velocity of 7.5 km s^{-1}, which increased to a peak of 7.8 km s^{-1} at closest approach due to the gravitational pull of the Earth. Figure 2 shows a diagram of the close approach. The orbital perturbations during the encounter lowered the semimajor axis to 2.09 au and the orbital period to 3.0 yr, thus injecting 2023 DZ2 into a 3:1 mean resonance with Earth. Based on the background close approach frequency for the asteroid population (Farnocchia & Chodas 2021), objects with an absolute magnitude brighter than 2023 DZ2's ($H = 24.3$) come this close to Earth roughly once per decade, on average.

For a few days after its discovery was announced by the MPC, 2023 DZ2 had a nonnegligible probability of an Earth impact in 2026 March. On 2023 March 16, based on the La Palma observations from the discovery MPEC, JPL's Sentry impact monitoring system[48] computed an impact probability of 0.01%. On March 17, 25 new observations were published in MPEC 2023-F20, and as a result, the impact probability

[46] MPEC 2023-F12: https://www.minorplanetcenter.net/mpec/K23/K23F12.html.

[47] https://ssd.jpl.nasa.gov/tools/sbdb_lookup.html#/?sstr=2023dz2

[48] https://cneos.jpl.nasa.gov/sentry/

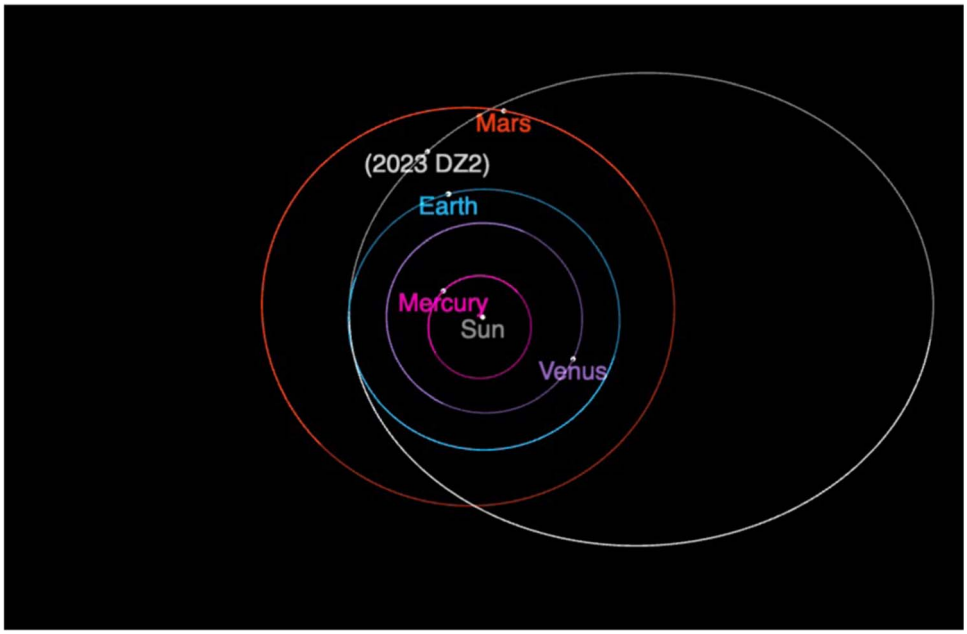

Figure 1. Heliocentric osculating orbit of 2023 DZ2 viewed from the northern ecliptic pole.

increased to 0.17%, corresponding to a Palermo scale (Chesley et al. 2002) of −1.1 and a Torino scale (Binzel 2000) of 1. On March 18, 43 additional observations were published in MPEC 2023-F30,[49] including precoveries from Pan-STARRS 2 (station code F52), Kitt Peak-Bok (V00), and the Mt. Lemmon Survey (G96) as far back as 2023 January 14. The probability slightly increased again to 0.23%. Finally, the trend reversed on March 19 with 39 follow-up observations from MPEC 2023-F48,[50] which lowered the impact probability to 0.001%. As new observations were reported in the following days, including radar astrometry[51] as presented in Section 7 here, the possible impact in 2026, as well as any other impact over the next 100 yr, was completely ruled out.

3. Photometry

After the discovery announcement of 2023 DZ2 on 2023 March 16 by the MPC, photometric observation requests to the community were initiated by the IAWN Campaign Coordinator via the official IAWN mailing list on 2023 March 19. Over the course of the 10 days that followed, campaign observations were acquired by the community from sites on six continents spanning a wide range in both latitude and longitude. The observations (almost 30 observers/telescopes and ∼8000 data points) that comprise the photometric campaign are summarized in Table 1.

Data were reduced by each contributor using their own preferred pipeline and provided to the campaign in calibrated apparent magnitude. The top panel of Figure 3 shows all campaign data in the various photometric filters in apparent magnitude. 2023 DZ2 had an apparent magnitude of ∼19 when the campaign started and peaked at a magnitude of around 11 at the closest approach to Earth on 2023 March 25 (approximately one week into the campaign) and subsequently grew fainter again, as can be seen in the top panel of Figure 3. Because the asteroid made a relatively close flyby (the minimum distance to Earth was 0.00117 au or 175,000 km), with varying Earth–Sun–asteroid observing geometries and Earth–asteroid distances (δ), all observing times were corrected for light travel time, and the apparent magnitudes were converted to absolute magnitudes before any analysis on the photometric data was performed. The middle panel of Figure 3 shows all data in reduced magnitude, where the magnitude's dependence on δ has been removed and the reduced magnitudes plotted as a function of the phase angle, α (Sun–target–observer angle).

At the start of the campaign, the phase angle was around 60° and reduced slowly for several days to ∼50° and then more rapidly 24 hr before the close approach, reaching a minimum of >5° a few hours before the closest approach. After the close approach, the phase angle increased rapidly again, reaching ∼100°. The asteroid had a plane-of-sky rate of motion of $>4''$ s^{-1} for a 24 hr window around the closest approach, making observation and photometric reduction challenging for non-expert asteroid observers. Therefore, the majority of data collected before the close approach were at a phase angle between 50° and 60° and after close approach at ∼100°. The solid line shown in the middle panel of Figure 3 also shows the *H–G* model fit formulated by Bowell et al. (1989) and summarized in Dymock (2007), and the bottom panel of Figure 3 shows the phase angle dependence on the magnitude (from the *H–G* model fit) removed, i.e., the absolute magnitudes, *H*. The absolute magnitudes were used for all further analyses discussed here. Very few data were collected during the campaign at a phase angle below 50°, which makes the *H–G* model fit somewhat unreliable. Hence, we make use of the JPL value for H_V, $\alpha = 0$ of 24.3, which is based on an assumed $G = 0.15$, throughout the manuscript for consistency. However, an attempt at a fit to the campaign data results in a value for *G* of 0.46 ± 0.23 for 2023 DZ2 that hints toward an E-type asteroid (*G* values of around 0.5 for E-types is suggested by Shevchenko et al. 2003).

The asteroid colors from the campaign were calculated by using the median magnitude of the combined data in a specific

[49] https://www.minorplanetcenter.net/mpec/K23/K23F30.html
[50] https://www.minorplanetcenter.net/mpec/K23/K23F48.html
[51] https://ssd.jpl.nasa.gov/sb/radar.html

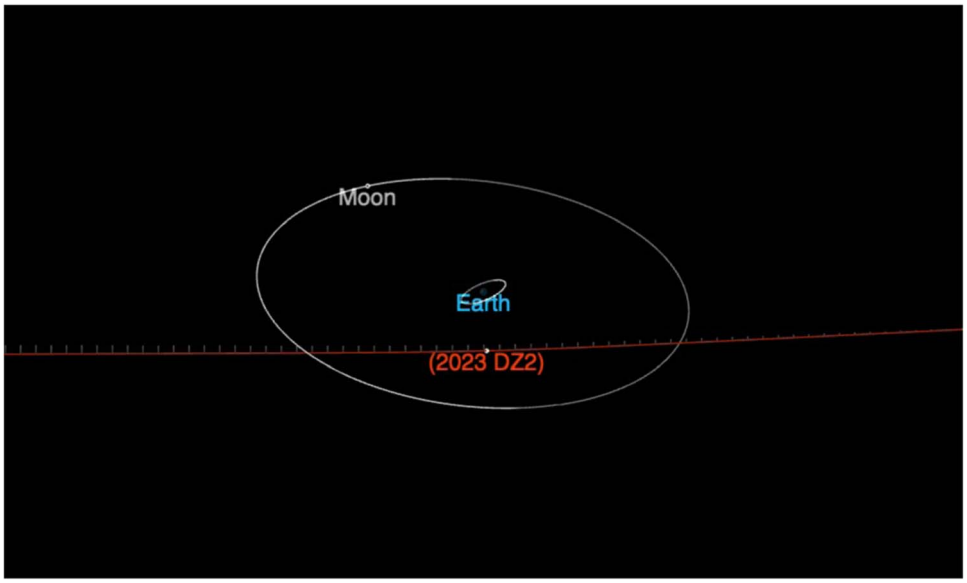

Figure 2. Diagram of the 2023 March 25 close approach of 2023 DZ2 to Earth. The relative velocity at closest approach is 7.8 km s^{-1}. 2023 DZ2 moves from left to right in this plot.

filter relative to the median magnitude value for all the *g*-filter data. The relevant values calculated were $V–R = 0.413 \pm 0.006$, $V–I = 0.800 \pm 0.007$, $g–r = 0.488 \pm 0.006$, $r–i = 0.202 \pm 0.008$, and $i–z = 0.180 \pm 0.011$. The *V–R* and *V–I* colors closely resemble those of a typical X taxonomic type asteroid with *V–R* and *V–I* colors reported in the literature of ∼0.41 and ∼0.81, respectively (Dandy et al. 2003; Erasmus et al. 2018). The campaign *g–r* and *r–i* colors also match those of literature values of ∼0.5 and ∼0.2, respectively, for a typical X-type asteroid (Janse van Rensburg 2021) and are similar within the uncertainty to the colors reported by and an independent study of 2023 DZ2 by Popescu et al. (2023), who reported colors of $g–r = 0.555 \pm 0.055$ mag, $r–i = 0.154 \pm 0.055$ mag, and $i–z_s = 0.064 \pm 0.059$.

Before performing any rotation period analysis, all filter data were offset to match the *g*-filter magnitudes by subtracting/adding the relevant colors (see previous paragraph). After the normalization to *g*-filter magnitudes, a rotation period search was performed on the entire photometry data set with the SciPy (Virtanen et al. 2020) implementation of the Lomb–Scargle (LS) method (Lomb 1976; Scargle 1982). The resulting LS periodogram is shown in the top panel of Figure 4, which shows the strongest periodogram peak at a rotation period of $P = 6.2745 \pm 0.0030$ minutes. The entire campaign's photometry data set (∼8000 data points), folded at that best-fit period, is shown in the bottom panel of Figure 4. The relatively large scatter still visible in the folded data is due to the light-curve amplitude variability as a function of observing geometry across the campaign (there is a >100° phase angle spread in the campaign data set). The average light-curve amplitude of the campaign data is 0.504 ± 0.057 mag (see bottom panel of Figure 4).

4. Spectroscopy

Visible spectra were obtained using the OSIRIS spectrograph on the Gran Telescopio Canarias (GTC) and the Robotic Automated Pointing Telescope for Optical Reflectance Spectroscopy I (RAPTORS I) on 2023 March 20 and March 25, respectively. The GTC/OSIRIS observations are described in Popescu et al. (2023). The RAPTORS I observation (0.45–0.93 μm) used a 30 lines mm^{-1} diffraction grating with a spectral resolution of $R \sim 30$ at 0.45 μm.

Two independent observing programs obtained near-infrared spectra (0.7–2.5 μm) on 2023 March 25 using the SpeX instrument (Rayner et al. 2003) on the NASA Infrared Telescope Facility (IRTF). Both observing groups (MITHNEOS and Reddy) used similar observing setups and strategies. Spectra were obtained in low-resolution prism mode with a 0.″8 slit width. The slit was oriented along the parallactic angle to minimize the effects of differential atmospheric refraction. The MITHNEOS program used a known solar standard for the telluric band correction (e.g., Binzel et al. 2019). The Reddy program observed a G-type local extinction star before and after the asteroid. Additionally, they obtained near-IR spectra of a solar analog to correct for possible spectral slope variations introduced by the extinction star. Observational circumstances for the four spectra are presented in Table 2.

RAPTORS I spectral data were reduced using a reflectance spectroscopy pipeline written in Python following the procedure described in Battle et al. (2022). The MITHNEOS spectrum was reduced via their standard procedure (Binzel et al. 2019) of IRAF and IDL routines. An atmospheric transmission model (ATRAN; Lord 1992) is used for the final telluric correction. The Reddy spectrum was reduced using the IDL-based software Spextool (Cushing et al. 2004) following the steps described in Sanchez et al. (2013, 2015).

The visible and near-IR spectra were combined in pairs, and both sets of spectral were normalized to unity at 1.5 μm (Figure 5; spectra are offset vertically for clarity. Both spectral pairs fall within the X-complex (DeMeo et al. 2009). The X-complex is a degenerate group that includes the E, M, and P taxonomic classes, which can be distinguished by albedo. The lack of a thermal tail in the near-infrared observations during the object's close approach (heliocentric distance of ∼1 au) immediately indicated a moderate-to-high albedo. We can use complementary observations from the other working groups to conclude that this object is likely an E-class asteroid. Our conclusion is supported by the weak (2% depth) 0.9 μm feature

Table 1
Observational Circumstances for Photometric Observations

Observatory/Telescope	Aperture (m)	Location (Obs. Code)	Filters	No. of Data Points
Teide Observatory (TTT)	0.80	Spain (Y65)	V	900
SONEAR Observatory	0.45	Brazil (Y00)	clear$_V$	784
Calar Alto Observatory	0.80	Spain (Z84)	g', r', i', z'	760
Kryoneri Observatory	1.20	Greece (L10)	R and I	640
Berthelot Observatory	0.38	Romania (L54)	clear$_V$	503
GAL Hassin Observatory	0.40	Italy (L34)	g', r', i'	426
La Silla Observatory (TRAPPIST–South)	0.60	Chile (I40)	R	400
Montsec Observatory	0.80	Spain (C65)	V, R, I	359
Tenerife Observatory and Cerro Tololo Inter-American Observatory (LCO)	1.0	Spain (Z24), Chile (W86)	w_{PI}	352
Oukaïmden Observatory (TRAPPIST-North)	0.60	Morocco (Z53)	R	350
Northold Branch Observatory	0.25	UK (Z80)	clear$_R$	340
La Silla Observatory (Danish Telescope)	1.54	Chile (W74)	V and R	309
Kourovka Astronomical Observatory	0.40	Russia (168)	R	216
Pistoia Mountains Astronomical Observatory	0.60	Italy (104)	V, R, and clear$_R$	207
Bucharest Astronomical Observatory	0.50	Romania (073)	clear$_V$	174
Zadko Observatory (C14)	0.36	Australia (D20)	g' and clear$_V$	164
NAC Observatory	0.35	USA (U98)	clear$_{r'}$	136
South African Astronomical Observatory (Lesedi)	1.0	South Africa (M28)	g', r', i'	113
Teide Observatory (ATLAS-Prototype)	0.46	Spain (954)	clear$_V$	80
NOAK Observatory	0.25	Greece (L02)	clear$_G$	74
Beato Ermanno Observatory	0.30	Italy (L73)	V and R	50
Beppe Forti Astronomical Observatory	0.40	Italy (K83)	clear$_R$	39
Haleakala Observatory and El Sauce Observatory (ATLAS)	0.50	USA (T05), Chile (W68)	o	18
NAOC-Xinglong	0.70	China (P22)	clear$_G$	11
NAOC-Korla	0.60	China (N83)	clear$_G$	8
HOB Observatory	0.20	Italy (L63)	B, V, R	3

seen in the Reddy SpeX data. This feature has been linked to low-Fe pyroxene (e.g., Clark et al. 2004). The MITHNEOS SpeX and GTC OSIRIS data do not show the same feature due to the lower signal-to-noise ratio (SNR) of those data sets. It is interesting to note that near-IR spectra do not show the rise in reflectance past 2.0 μm due to thermal tail of the Planck curve. This lack of detection of a thermal tail in both the lower- and higher-SNR near-IR data sets is another first-cut assessment that the object's albedo was relatively high and provides a constraint on its albedo independent of other techniques.

5. Thermal Infrared Photometry and Optical Polarimetry

Direct measurement of the physical properties of an asteroid is important for removing uncertainties that arise in hazard calculations when using assumed values, for example, albedo. The diameter of an object can be obtained from thermal infrared radiometry, stellar occultations, or radar ranging, while the albedo can be directly probed using polarimetry. Each of these techniques have their own complications and specific restrictions on when these data can be obtained, so it is important that the community maintain a suite of capabilities to be able to rapidly respond to unknown targets, as was needed for the case of 2023 DZ2. For example, while the NEOWISE mission (Mainzer et al. 2014) has produced the largest set of infrared-determined diameters for asteroids, it can no longer target a specific object but rather conducts a scan of the sky that is fixed by its orbit. Due to this fixed pattern and the asteroid's high rate of motion, NEOWISE did not observe 2023 DZ2 during its close pass, with the object missing the field of view of the closest exposure by $\sim 7'$. Instead, we were able to call upon the MIRSI instrument on the NASA IRTF for rapid thermal infrared characterization of 2023 DZ2. Similarly, the Torino Polarimeter (ToPol) instrument on the Calern 1.04 m telescope was able to provide rapid polarimetric characterization.

5.1. ToPol Polarimetry

We conducted optical polarimetric observations of 2023 DZ2 using ToPol on 2023 March 24. The ToPol instrument is installed on the Cassegrain focus of the 1.04 m Omicron telescope, which is part of the C2PU facility at the Calern Observatory located in the South of France (MPC code 010). ToPol uses a wedged double Wollaston design that permits full determination of the Stokes I, Q, and U parameters in a single acquisition. More information about ToPol is provided by Pernechele et al. (2012) and Devogele et al. (2017), while Bendjoya et al. (2022) give a recent update on all the observations performed with ToPol.

For airless bodies, the linear degree of polarization is computed as the difference between the intensity of the light having its polarization oriented perpendicular to the scattering plane (i.e., the plane containing the Sun–object–observer) and the intensity of the light having its polarization oriented in the scattering plane. This value is then normalized by the sum of the same parameters. Often referred to as Pr, this parameter is negative if the polarization is found to lie in the scattering plane or positive if it is perpendicular to it. See Belskaya et al. (2015) for a review and more information about asteroid polarimetry.

The observed linear degree of polarization for asteroids is directly influenced by the phase angle, which represents the angle between the Sun, the asteroid, and the observer. When the phase angle is small (typically $<20°$), the polarization aligns with the scattering plane (Pr < 0). As the phase angle increases, the polarization orientation shifts to align with the perpendicular to the scattering plane (Pr > 0), with a transition point known as the inversion angle ($\alpha 0$) typically occurring around $\alpha \sim 20°$. The minimum, maximum, and slope of this

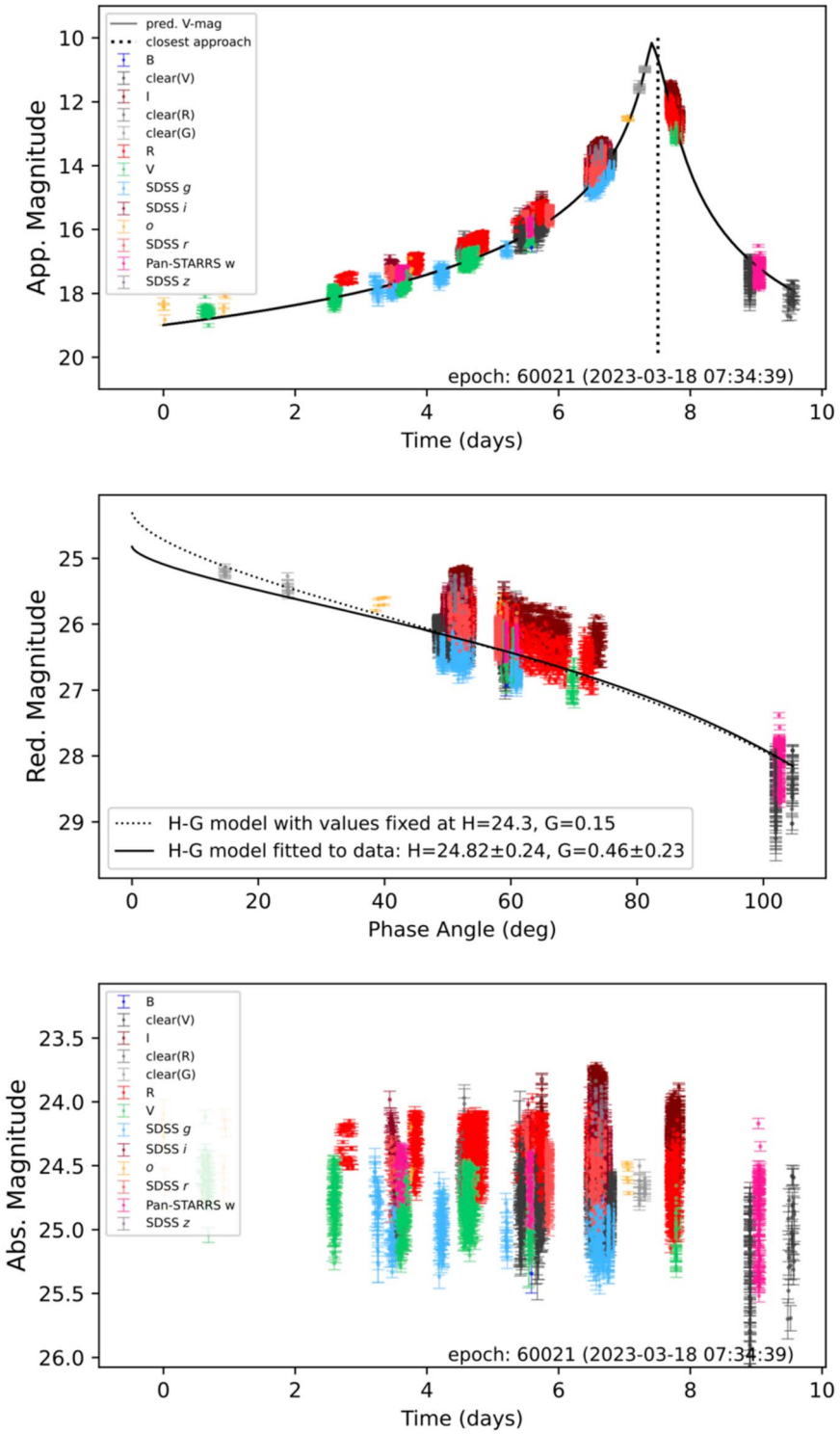

Figure 3. (Top) The raw photometric data of 2023 DZ2 in apparent observed magnitude showing all data collected in the campaign with the various photometric filters used indicated with different plotting colors (see legend). The vertical dotted line shows the time of closest approach when 2023 DZ2 reached its peak brightness. (Middle) Reduced magnitude with the observer-to-object distance dependence on the brightness removed. Two *H*–*G* model curves are shown, one with the *G* and *HV*, $\alpha = 0$ values fixed to 24.3 and 0.15, respectively, obtained from JPL and the other an attempt at fitting the *H*–*G* model to the photometry data collected during the entire campaign. We only fit the *V*-filter data together with the *g* and unfiltered data (calibrated in the *V* and *G* bands) since the *V*–*g*, *V*–clear*V*, and *V*–clear*G* colors for the campaign data were only −0.23, 0.01, and 0.12 mag, respectively (i.e., $V \approx \mathrm{clear}V \approx \mathrm{clear}G \approx g$). The fitted values for *G* and *HV*, $\alpha = 0$ values are 24.82 ± 0.24 and 0.46 ± 0.23, respectively. (Bottom) Evolution of absolute magnitudes of 2023 DZ2 for the entire campaign as a function of time.

curve are correlated with the reflectivity of the surface material (Cellino et al. 2015), with high polarization values measured for low-albedo objects while low polarization values are measured for high-albedo objects. As such, polarimetric characterization can be used as a direct constraint on an asteroid's surface reflectivity properties, with low-albedo objects providing stronger constraints due to their larger polarimetric signal and larger comparison set.

We obtained 112 individual measurements of 180 s each for 2023 DZ2 between 2023 March 24 19:41 UTC and 2023

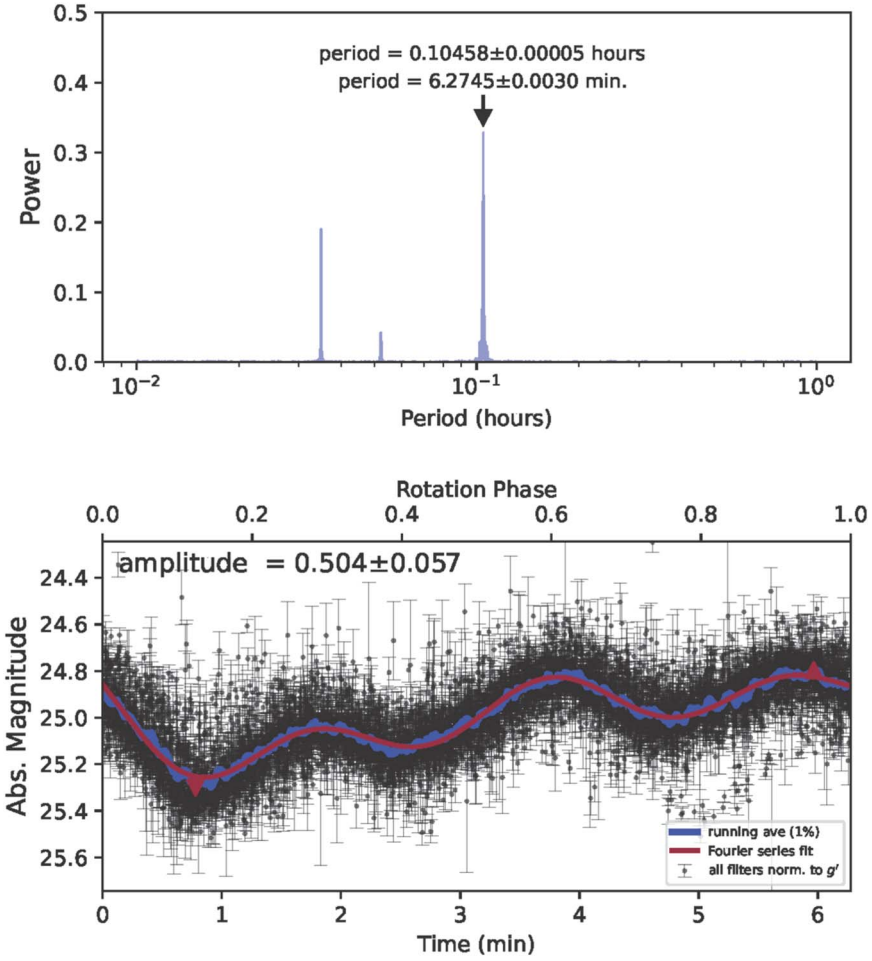

Figure 4. (Top) The LS periodogram of the combined filter data (see Section 3). The arrow shows the strongest periodogram peak and the rotation period labeled. The rotation period is 6.2745 ± 0.0030 minutes. (Bottom) The combined filter data (from the derived colors; see Section 3) are folded with the best period solution (shown in the top panel) and a Fourier series fit shown as a solid burgundy line. The burgundy triangles show the minimum and maximum values of the fit and are used to determine the light-curve amplitude displayed in the top left corner of the panel.

March 25 01:26 UTC. During that period, the phase angle ranged from 53.°1 to 49.°4, and the *V* magnitude ranged from 14.5 to 13.9. We combined all the observations to derive a single determination of the linear degree of polarization $\mathrm{Pr} = 1.64\% \pm 0.05\%$. Comparing with other asteroids for which polarization and albedo information is available at similarly high phase angles, we see that low-albedo asteroid (3200) Phaethon displays a linear degree of polarization around ∼11% (Devogele et al. 2018), while high-albedo asteroids 1998 WT24 and 2010 XC15 display polarization like 2023 DZ2 around ∼1.5% (Beniyama et al. 2023). Based on these comparisons, we can infer that the albedo of 2023 DZ2 is like that of 1998 WT24 and 2010 XC15. The different albedo determinations for 1998 WT24 are 0.27, 0.35, 0.5, or 0.59 by Delbo (2006); 0.654 by NEOWISE (Mainzer et al. 2019); and 0.816 by ExploreNEOs (Trilling et al. 2010). We can thus estimate that the albedo of DZ2, based on polarization only, should be $p_V = 0.5 \pm 0.2$, consistent with an E-type taxonomy. A larger survey of NEO polarizations at high phase angles would allow for more comparison objects and thus improved albedo constraints using this technique.

5.2. MIRSI Observations

2023 DZ2 was observed as a target of opportunity on the NASA IRTF MIRSI instrument on 2023 March 25. Simultaneous optical and thermal observations of 2023 DZ2 were conducted on 2023 March 25 05:00 UTC while the asteroid was 0.002 au from Earth and at a visual magnitude of 13.18. We used the Near-Earth Asteroid Thermal Model (NEATM; Harris 1998) to provide an estimate of what the brightness of the object would be at mid-infrared wavelengths by assuming a wide range of possible diameters and albedos consistent with the major taxonomic classes. 2023 DZ2 was predicted to have a thermal flux within the range of 1.3–8.1 Jy at 10.5 μm (i.e., the center wavelength of the *N*-band filter). Optical observations obtained during planning showed that the object had a rapid rotation period of $P < 10$ minutes (see Section 3), which implied that a Fast Rotator Thermal Model (FRM; Lebofsky & Spencer 1989) should be used for thermal flux predictions. The FRM provided a predicted asteroid flux in the range of 0.3–2.2 Jy during the time of the observation.

Observations of 2023 DZ2 were obtained using MIRSI's *N*-band filter for infrared characterization, as well as simultaneous acquisition of *R*-band optical data with MIRSI's optical camera (MOC). We reduced the *N*-band data using the MIRSI reduction pipeline, which will soon be publicly available (J. Hora, private communication). To calibrate the 2023 DZ2 *N*-band measurements, we observed the standard star Alpha Hydrae before, during, and at the end of the observation to properly correct for sky variations. The MOC data were

Table 2
Observational Circumstances for Spectroscopic Data

Telescope	Date (UT)	Time (UT)	V mag	Solar Analog
GTC	2023 March 20	22:00	18.2	SA 98-978 and SA 102-1081
RAPTORS I	2023 March 25	4:15	13.2	HD 129357
IRTF/ MITHNEOS	2023 March 25	8:36	12.9	SA 98-978
IRTF/Reddy	2023 March 25	8:19	12.7	SAO 120107

reduced using a reduction pipeline that will also be publicly available (A. Lopez-Oquendo, private communication). The MOC data were used in conjunction with other ground-based data for the photometry campaign of 2023 DZ2 (see Section 4). We measured an N-band flux of 220 ± 33 mJy (1σ uncertainty), which is significantly lower than predicted, suggesting that 2023 DZ2 has a smaller size and higher albedo than the range used for predictions (10%–50%).

To constrain the best-fit diameter and albedo for 2023 DZ to our observations, as well as the associated uncertainties on each parameter, we used a Monte Carlo approach to explore various sources of uncertainty, which include uncertainty in the measured flux, calibration uncertainty assumed to be ~10%, and uncertainty in the absolute H_V magnitude, all while fitting the FRM to our 10.5 μm observations. Orbital geometry was obtained from the JPL Horizons system, with 2023 DZ2 having a heliocentric distance of 0.999 au, a geocentric distance of 0.002, and a phase angle of 44.°037 at the time of observation. We assumed an absolute magnitude $H_V = 24.82 \pm 0.24$, as derived from the photometry campaign (see Figure 3). In our Monte Carlo approach, we assumed a Gaussian distribution of H with a spread around the 0.24 mag uncertainty and generated 106 possible synthetic fluxes, fitting each one to retrieve the 16th, 50th, and 84th percentile values. We obtained a best-fit diameter of $22_{+4/-3}$ m, which gives an albedo of $0.49_{+0.29/-0.32}$. The derived albedo agrees with the expected range for E-type asteroids and is consistent with the spectroscopic observations described above.

6. Radar Observations

Following the announcement of the discovery of 2023 DZ2 (MPEC 2023-F12), our "MPEC Radar SNR" script automatically estimated possible radar SNRs at Goldstone and indicated that SNRs would be very strong in late March of 2023. The discovery announcement provided about one week of advance notice. The view periods did not overlap any previously scheduled targets, when it would have been straightforward to repurpose time for a newly discovered object, so we requested several tracks on the 70 m DSS-14 antenna at Goldstone and were able to obtain two tracks on 2023 March 25 and March 27 at times that straddled the closest approach. When we made the requests on 2023 March 17, the impact probability for 2026 was still rising, but by the time the Goldstone tracks were finalized late on 2023 March 20, the impact probability had become vanishingly small.

We also notified S. Horiuchi et al. in Australia, and they promptly requested time at the Deep Space Network antennas at Canberra to transmit and the Australia Telescope Compact Array (ATCA) to receive. Tracks on the 34 m DSS-35 and DSS-34 antennas in Australia were scheduled on 2023 March 24 and 25 at times when Goldstone was not available for this campaign. The asteroid's approach was close enough that it would have been possible to transmit at the 34 m DSS-13 antenna at Goldstone and obtain 1.875 m resolution images by receiving at the Green Bank Telescope, but this was not possible because Green Bank was offline for maintenance. DSS-13 had also been offline due to damage sustained on the control building roof during winter storms, but temporary repairs were completed in time to use DSS-13 to receive transmissions from DSS-14 on 2023 March 25.

6.1. Overview of the Radar Observations

Radar observations began on March 24 at Canberra, continued on 2023 March 25 at Goldstone and Canberra before closest approach, and concluded on 2023 March 27 at Goldstone. Attempts to obtain radar echoes in Australia on 2023 March 24 were unsuccessful, apparently due to the distance, which varied between 0.0059 and 0.0054 au. The Canberra observations on that day used the 34 m DSS-35 antenna transmitting 20 kW at 7160 MHz (4.2 cm) and received with the six-element ATCA, which has an effective collecting area of a single 49 m antenna.

Radar observations at Goldstone on 2023 March 25 were unusually challenging due to the very short round-trip light travel time and the time it takes during monostatic observations to switch between transmitting and receiving. Goldstone equipment and software take about 2 s to switch, but we seldom attempt monostatic observations of asteroids that are this close, and we had to modify software to make this work. The round-trip light travel time when the Goldstone observations started was 3.2 s. To take data without causing equipment and software problems, we padded the monostatic data acquisition by sampling noise during each transmit/receive cycle. This was successful and enabled us to see radar echoes within seconds of when the observations began. We used the echo power spectra on 2023 March 25 to estimate Doppler corrections to the ephemerides, echo bandwidths, and circular polarization ratios but not for estimation of radar cross sections because noise padding corrupted the reduction. We obtained reliable radar cross sections using monostatic observations with significantly longer round-trip times (7–8 s) on 2023 March 27, when noise padding was not necessary.

During the Goldstone track on 2023 March 25, the distance decreased from 0.0033 to 0.0020 au. The radar SNRs are proportional to $1/R^4$, where R is the radial distance, so the reduction in the asteroid's distance corresponded to a sevenfold increase in the SNRs. The shrinking round-trip light travel time also caused increasingly challenging circumstances for monostatic observations, which have a hard limit of 2.1 s (providing only 0.1 s of data), so after obtaining ranging measurements, which are better calibrated if the observations are monostatic, we switched to bistatic observations, where we transmit continuously with DSS-14 and receive continuously with DSS-13.

The bistatic configuration simplifies observations for very close and/or slowly rotating objects, and it reduces the SNRs by a factor of several, but the SNRs were so strong with 2023

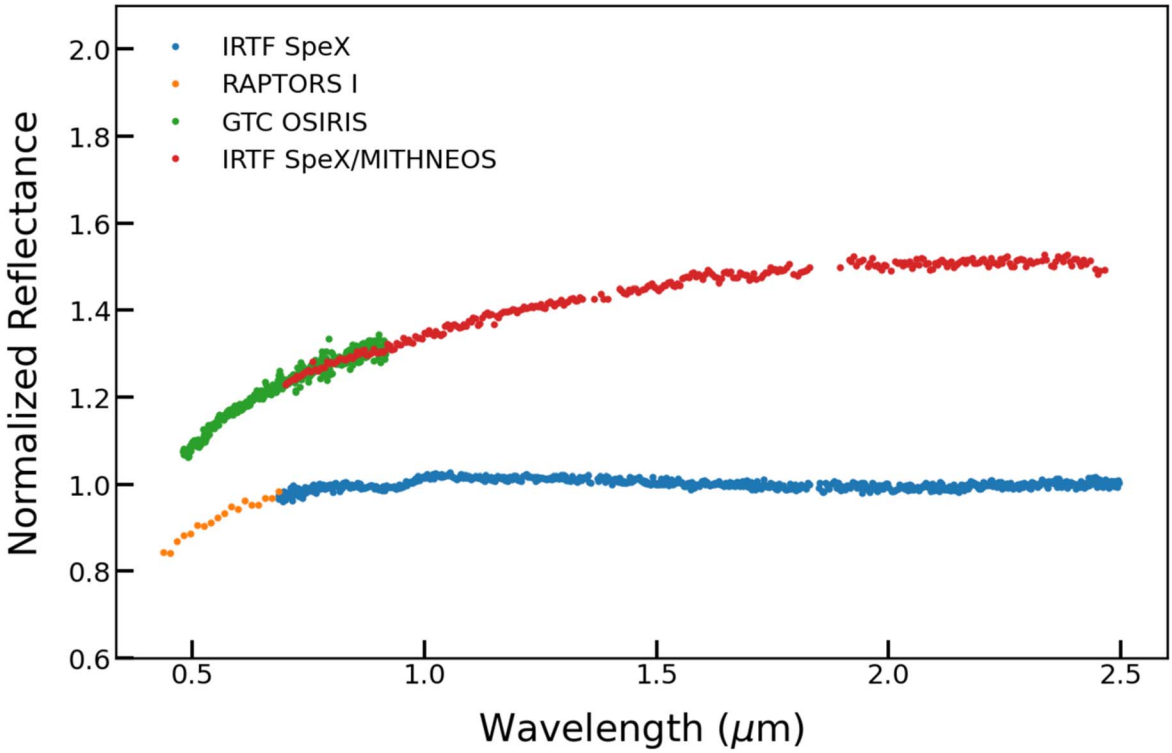

Figure 5. Visible and near-infrared spectra of 2023 DZ. The top spectrum combines spectra from GTC OSIRIS and NASA IRTF SpeX instruments. The bottom spectrum is visible and near-IR data from RAPTORS I and NASA IRTF SpeX. A weak 0.9 μm absorption feature due to pyroxene is visible in the bottom higher-SNR spectrum from the NASA IRTF.

DZ2 that this was not a problem. We conducted detailed delay-Doppler imaging for 3.9 hr that covered about 37 rotations by the asteroid. We did also extensive continuous-wave (CW) observations to help multiple antennas in Australia and Japan receive echoes. The 2023 March 25 observations lasted nearly 7 hr, and due to the rapid 0.105 hr rotation period, the track spanned more than 60 rotations. The 2023 March 25 Goldstone and Canberra observations occurred as the asteroid was inbound and did not encompass the time of closest approach.

6.2. Orbit Refinement

We used monostatic observations on 2023 March 25 to obtain a detection and estimate a Doppler correction and update the orbital solution. We then obtained multiple ranging (i.e., time delay) measurements at progressively finer resolutions, updated the orbital solutions, and shrank the 3σ time delay uncertainty by a factor of ~350. By 2023 March 27, after the closest approach, the 3σ time delay uncertainties had increased by a factor of about 200 relative to those obtained with our final orbital solution on 2023 March 25, so we obtained additional radar astrometry early in the track, updated the orbital solution, obtained CW data to estimate calibrated radar cross sections, and then devoted the rest of the track to imaging with a resolution of 3.75 m.

6.3. Results

The CW echoes on 2023 March 25 yielded a bandwidth of 20 Hz (Figure 6). The expression for an echo's bandwidth is given by

$$B = 4\pi D \cos(\delta)/(\lambda P),$$

where D is the diameter, δ is the subradar latitude, λ is the radar wavelength, and P is the rotation period. If the object has significant elongation, then the bandwidth will vary as it spins. The first CW observations spanned ~13.5 minutes, which is more than two rotations, and sampled the maximum range of bandwidths possible as the asteroid rotates. Given that P is known, the estimation of the bandwidth places a lower bound on the maximum pole-on breadth $D_{\max}$. If we adopt $B = 20$ Hz and $P = 0.105$ hr, then we obtain $D_{\max} = (21\text{ m})/\cos\delta$. This is smaller than expected given the absolute magnitude and could indicate that the asteroid is less than 50 m in diameter and/or that the subradar latitude was well away from the equator, which reduces the bandwidth.

The shapes of the echo power spectra can provide information about the shape of the asteroid, such as its elongation as it rotates, so we checked spectra that covered more than one rotation but found that the bandwidths varied by only about ~10%. The implication is that 2023 DZ2 is not substantially elongated. The echo in Figure 6 has a pronounced dip in the middle that hints at a concavity. However, even though the integration covers more than 13 minutes, data-taking problems caused by the very short round-trip time produced many data dropouts with empty data files. Consequently, the echo in the figure is a weighted sum of a small number of runs and has considerable "speckle" at frequencies with echo power (Ostro 1993). Thus, the dip may be self-noise and not due to the asteroid's shape. We checked delay-Doppler images obtained later at the same orientations, when there were no data acquisition problems, and did not see a large dip.

Echoes were obtained on 2023 March 25 at the ATCA using transmissions from DSS-34 at Canberra (Figure 7). These data were obtained shortly after the Goldstone observations concluded but several hours prior to the closest approach. The echo bandwidth is consistent with results obtained at

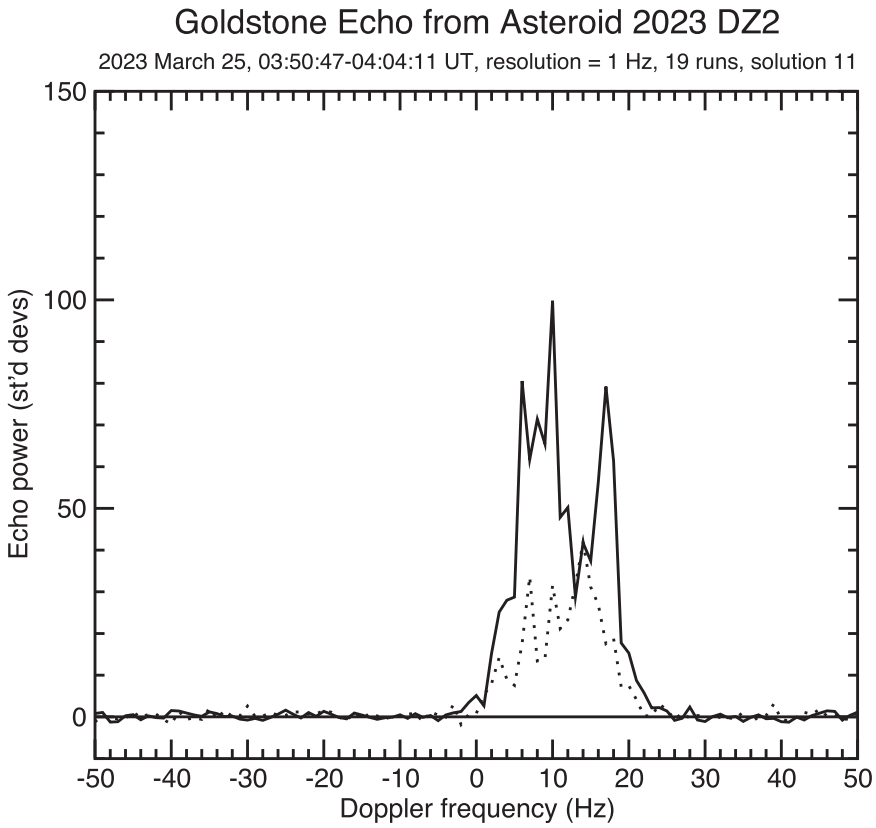

Figure 6. Echo power spectra obtained on March 25 of 2023 DZ2 using the 70 m DSS-14 antenna at Goldstone to transmit and receive. Echo power in standard deviations of the noise is plotted as a function of Doppler frequency using JPL/Horizons solution 11. The solid curve denotes echo power in the opposite sense of circular polarization relative to that transmitted, and the dashed curve shows echo power in the same sense. The frequency resolution is 1.0 Hz, and the figure shows a weighted sum of 19 runs.

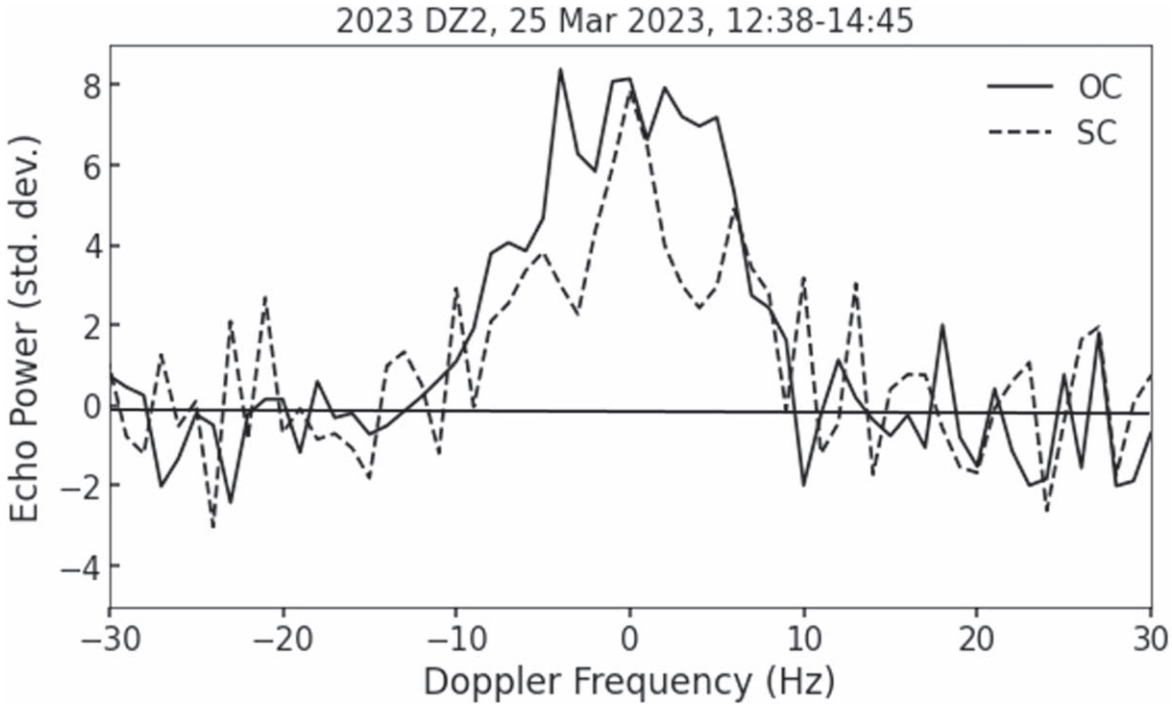

Figure 7. Echo power spectrum obtained on March 25 of 2023 DZ2 using the 34 m DSS-34 antenna at Canberra to transmit and the ATCA to receive. Notation is the same as in Figure 4. This shows an integration of 2.1 hr at a frequency resolution of 1.0 Hz.

Goldstone when the difference in the transmitter frequencies (7160 MHz versus 8560 MHz) is considered. An important reason to update the ephemeris early in the track was to reduce the drift of the echoes during delay-Doppler imaging. For imaging at Goldstone's transmitter frequency of 8560 MHz, a Doppler offset of +1 Hz to the ephemeris corresponds to −0.42

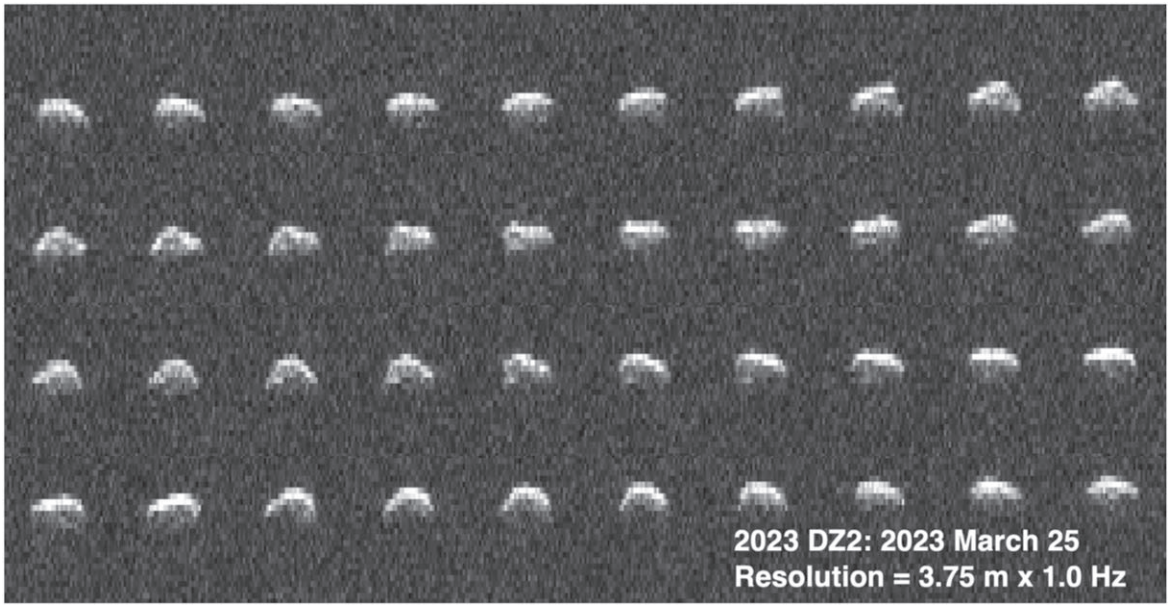

Figure 8. Collage of delay-Doppler images of 2023 DZ2 obtained on March 25 using the DSS-14 antenna at Goldstone to transmit and DSS-13 to receive. In each panel, time delay (range) increases downward and Doppler frequency increases to the right, so rotation is counterclockwise. Each row corresponds to 3.75 m (0.025 msec). The resolution in Doppler frequency is 1.0 Hz. Each image is an integration spanning 10 s and corresponds to about 10° of rotation.

μs of drift per hour (Ostro 1993). The SNRs were strong enough to obtain images with a time delay resolution of 0.025 μs (3.75 m), and a Doppler correction of 1 Hz would produce 17 rows of drift per hour, so we sought to reduce the Doppler uncertainties as much as possible. We shrank the Doppler uncertainties substantially, but a modest amount of drift is evident in the images. To overcome this, we used short integrations of only 10 s per data file during which drift was minimal. We also adopted short integrations to avoid excessive rotation by the asteroid: with a rotation period of 0.105 hr, a 10 s integration gives about 9.°5 of rotation.

Figure 8 shows the final 40 images we obtained at DSS-13 on 2023 March 25. They have a resolution of 3.75 m (0.025 μs) x 1.0 Hz and span somewhat more than one full rotation. Feature tracking confirms the 0.1 hr rotation period estimated from photometry. The delay-Doppler appearance of the asteroid changes considerably as it rotates: at some orientations the echoes appear rounded, at others the shape appears triangular, and we also see conspicuous flat regions oriented toward the radar. There is minor topography such as small concavities (on the scale of several pixels) and "bumps" evident at the level of 1–2 pixels. Delay-Doppler images reveal relatively modest variations of 10% in the bandwidths as the asteroid spins, a result consistent with that seen in echo power spectra.

If we count the number of rows with echo power and average them over one rotation, then we obtain visible range extents that average about five rows (19 m). If the object were a sphere, then the radar could illuminate one half of it, and we could reasonably assume that the diameter is double the visible extent. For 2023 DZ2, the shape is irregular, and we lack detailed constraints on the polar axis, so we conclude conservatively that the diameter is probably somewhat less than double the mean visible extent. Therefore, we estimate that the diameter is about 30 ± 10 m. This is broadly consistent with the size derived from the MIRSI observations with uncertainties. For a diameter $D = 0.03$ km, a rotation period $P = 0.105$ hr, and an equatorial view, we expect a bandwidth of about 30 Hz. The bandwidth we measured was about 20 Hz, which implies that the subradar latitude was several tens of degrees off the equator.

6.4. Disk-integrated Properties

Figure 9 shows an echo power spectrum obtained at Goldstone from a weighted sum of 59 runs on March 27. These data provide our best calibrations and were used to estimate an OC radar cross section s_{oc} = 8E-5 km^2 and a circular polarization ratio SC/OC $= 0.46 \pm 0.03$. We obtain an indistinguishable radar cross section using the results from Australia, but the circular polarization ratio has a larger value of about 0.8. If we adopt 30 m as the diameter, then this radar cross section corresponds to a relatively low radar albedo of 0.11. We can also use the diameter and the absolute magnitude of 24.1 to compute the optical albedo from

$$\log_{10} p_v = 6.244 - 2\log_{10} D - 0.4H,$$

where H is the absolute magnitude, p_v is the optical geometric albedo, and D is the diameter (Zellner 1979).

If we adopt $H = 24.1$ and $D = 0.03$ km, then we obtain an unusually bright optical albedo $p_v = 0.42$. Spectroscopy indicates that 2023 DZ2 is an X-class object, which is spectrally degenerate and could indicate E-, M-, or P-types. Thermal infrared observation did not show an excess at long wavelengths, which would be indicative of an optically dark object. Thus, we can exclude the optically dark P spectral class. If 2023 DZ2 were metallic, then we would expect a radar albedo larger than 0.3, but our nominal estimate of only ~0.1 probably rules out the M-class. The bright optical albedo and vis-IR spectrum are consistent with the E spectral class that is associated with the bright enstatite achondrite meteorites. However, previous radar observations of E-class NEAs (Benner et al. 1997, 2008; Virkki et al. 2022) with $H < 22$ have revealed that circular polarization ratios for the E-class have all exceeded 0.8. The value we obtain for 2023 DZ2 at Goldstone is significantly lower than previous estimates except

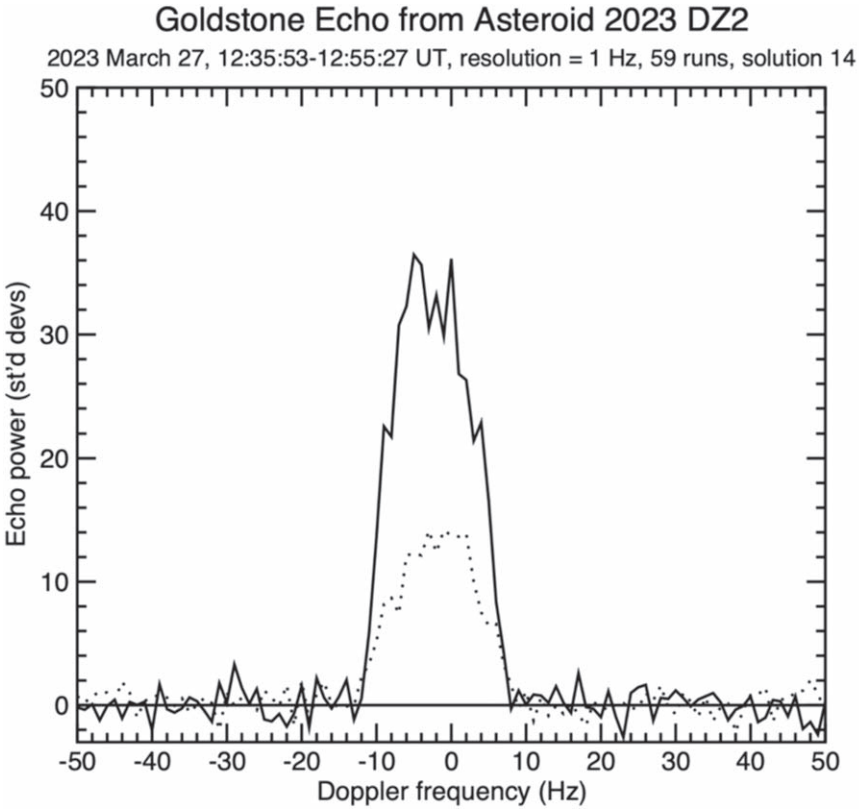

Figure 9. Monostatic echo power spectrum of 2023 DZ2 obtained at Goldstone on March 27. The resolution is 1.0 Hz, and the figure shows a weighted sum of 59 runs using JPL/Horizons solution 14. Notation is the same as in earlier figures.

for 2012 TC4, which is similar in diameter to 2023 DZ2, also an X-type, and with a similar circular polarization ratio (SC/OC = 0.55) and optical albedo of ~0.4 (Reddy et al. 2019). If 2023 DZ2 is an E-type object, then its near-surface environment may be significantly different from larger E-types previously observed with radar. Very few E-class objects <50 m in diameter have been studied in detail, so we do not know if 2023 DZ2 is an outlier or indicative of a real difference as a function of size.

7. Hypothetical Risk Assessment

Probabilistic assessments of the risk due to asteroid impacts have been performed to evaluate the overall risk due to the ensemble population of NEAs (e.g., Mathias et al. 2017; Rumpf et al. 2017; Stokes et al. 2017). The probabilistic asteroid impact risk (PAIR) assessment models and the approach used for these ensemble assessments also have been used to assess the hypothetical risk due to a single object as part of the IAWN observational campaigns of 2012 TC4 (Reddy et al. 2019), 1999 KW4 (Reddy et al. 2022a), and Apophis (Reddy et al. 2022b). Instead of using only generic asteroid properties and long-term impact frequencies representing the general asteroid population, these specific impact scenario assessments refine the property distributions based on the observational data obtained during the campaign. A similar risk assessment was done as part of the 2023 DZ2 observing campaign.

To support the analysis of the damage from a possible impact and assess the relevance of the observational data to that analysis, we considered a separate hypothetical scenario in which 2023 DZ2 had been on a trajectory leading to an impact in 2026. We selected one of the impact solutions initially found by Sentry, derived the orbital uncertainty based on the astrometric data collected for the real 2023 DZ2, and computed the corresponding impact probability. As of 2023 March 20.0 UTC, the hypothetical impact probability would have been 6%, with an impact corridor wrapping around the Earth from the Caribbean Sea to French Polynesia. Then, we updated the impact corridor to include all the astrometric data (both optical and radar) collected during the close encounter through 2023 March 28.0 UTC. At this point the impact probability would have reached 100%, with impact locations over northern Vietnam and southeastern China.

The risk of a hypothetical impact based on 2023 DZ2 was assessed for two epochs. The first assessment was based on the state of knowledge about the asteroid at the beginning of the campaign on 2023 March 20. The second assessment was based on the state of knowledge about the asteroid at the end of the campaign on 2023 March 28. A summary of the observationally determined properties utilized in each assessment is shown in Table 3. In order to simulate how risk assessments would proceed in a real-life scenario, the values used for each epoch are the current estimates on the epoch dates, which may vary from the final values discussed elsewhere in this paper. The PAIR model of Mathias et al. (2017) was combined with the affected population metrics defined by Stokes et al. (2017) to assess the risk at each epoch. The PAIR model utilizes a Monte Carlo framework to sample the range of possible impact locations and impactor physical properties. At each epoch, the risk assessment modeled the impact of 5000 asteroid property cases at each of 5000 hypothetical entry points, resulting in 25 million simulated impacts. The generation of the hypothetical entry points is

Table 3
Summary of the State of Knowledge during Each Epoch of Risk Assessment

Quantity	Epoch 1	Epoch 2
Date of assessment	2023 March 20	2023 March 28
Hypothetical impact probability	6%	100%
H magnitude	23.7 +/−0.4	24.2 +/−0.25
Diameter (m)	⋯	30 +/−10
Taxonomy	⋯	E-type

described in previous campaign papers (Reddy et al. 2019, 2022a, 2022b). The 5000 asteroid property cases were generated by an inference network that probabilistically samples from the distributions of likely asteroid properties based on available measurements, the distribution of the underlying population of NEAs, and the likely relationship between the properties.

The Epoch 1 properties were based on an absolute magnitude of 23.7 ± 0.4 based on the initial work by the photometry working group. All other properties were sampled from the distribution of the overall population of asteroids. For each property case, an absolute magnitude was chosen from a Gaussian distribution consistent with the initial measurement. An albedo was randomly chosen from the bimodal distribution of NEAs determined by Mainzer et al. (2011). The diameter for each case was calculated from the absolute magnitude and the albedo using the standard relationship. The resulting range of diameters within the 68% highest posterior density interval (HPDI) is 29–89 m, and the 99% HPDI range is 23–269 m. A likely taxonomy was assigned for each case based on the albedo and a simple application of the Bayes theorem, $P(T|p_v) \sim P(p_v|T) * P(T)$, where $P(p_v|T)$ is the measured albedo distribution for each taxonomy and $P(T)$ is the distribution of asteroids among the taxonomies. The distributions from DeMeo & Carry (2013) were used for $P(p_v|T)$ and $P(T)$. Each taxonomy was associated with a base density distribution appropriate for the related meteorites. Bulk densities were calculated by modifying the base densities using a broad macroporosity distribution as presented by Mathias et al. (2017). This resulted in a 68% HPDI range of asteroid masses from 8.4×10^6 to 7.1×10^8 kg and a 99% HPDI range of 7.3×10^6–1.9×10^{10} kg. The aerodynamic strength was distributed uniformly in log space in the range of 0.1–10 MPa (Popova et al. 2011). The aerodynamic strength was loosely linked to the porosity by quartiles, with the least porous quartile of cases being associated with the strongest strength quartile.

At Epoch 2, additional information was available from photometry about the absolute magnitude, from radar about the diameter, and from spectroscopy about the taxonomy. In this epoch, the property inference network started by sampling over the *H* magnitudes consistent with the photometric observations and the diameters consistent with the radar observations. An albedo was then calculated using the standard relationship between absolute magnitude and diameter. A base density was sampled based on the measured taxonomy. All other parameters were selected using the same procedure as the Epoch 1 properties. As a result of the characterization measurements, the 68% HPDI range of diameters and masses was reduced significantly to 23–39 m and 6.1×10^6–5.1×10^7 kg, respectively.

For each of the 25 million cases modeled in each epoch, the energy deposited in the atmosphere, the effective airburst altitude, any remaining energy striking the ground, and the coordinates of the impact or airburst along the entry trajectory atmospheric entry and breakup were determined from the Fragment Cloud Model of Wheeler et al. (2017). The extent of damage resulting from blast waves, thermal radiation, and tsunami was computed, and the number of people affected was calculated from the local population within the damage regions. For local blast and thermal damage, fractions of the affected population within the exposed regions were evaluated for four damage severity levels: serious (10% population), severe (30% population), critical (60% population), and unsurvivable (100% population). For tsunami, fractions of the population affected within the inundated region were determined based on flood depth. Given the size range of hypothetical impactors, no global effects were modeled. The total affected population for each case was taken as the largest population value among all the hazard sources.

Maps showing a subset of the possible damage regions for both epochs are shown in Figure 10. In Epoch 1, the possible impact points span from the Caribbean to French Polynesia. The most likely cause of damage is the blast, resulting in a 68% HPDI range in the size of the serious damage footprint from 0 to 26 km and a 99% HPDI range of 0–12,000 km. In Epoch 2, the possible impact points are focused over northern Vietnam and southeastern China. The most likely cause of damage remains the blast, but 86% of the cases result in no damage. The 99% HDPI range of the serious damage footprint is 0–270 km. Histograms of the affected population risks for each epoch are shown in Figure 11. Although the hypothetical impact probability between the two epochs increased from 6% to 100%, in this scenario the affected population risk significantly decreased from a 99% HDPI range of 0–2.2 meters to a range of 0–330,000 people. This decrease in risk was due to the improvement in the state of knowledge about both the impact corridor and the asteroid's physical properties. The final epoch's impact corridor did not include the high-population centers that the initial epoch's impact corridor crossed. In addition, the radar and spectroscopy measurements significantly constrained the diameter and mass ranges to the smaller end of the initial possible range.

8. Summary

The 2023 DZ2 campaign enabled us to learn several key lessons about our preparedness to respond to a hypothetical NEO impact hazard. We have summarized the lessons learned by each of the working groups below.

Photometry. We learned two key lessons as part of our photometric campaign of 2023 DZ2. The first is the lack of geographical coverage during close approach. As 2023 DZ2 made a close approach of the Earth, it was nighttime in Asia and Australia. But we obtained only a few photometric observations from these longitudes. Future campaigns should aim at encouraging observers from these longitudes to contribute data. The second lesson we learned is the nonuniformity of data formats and quality. Unlike astrometry, where the MPC sets standards for data format and quality, photometric observations of NEOs do not have a standard format. This has been a persistent problem in all of the IAWN campaigns, but we want to highlight the need for a standard format for photometric observations. One option to explore is the use of an online portal where data can be uploaded in a standard format with well-defined guidelines for reduction of data in a consistent manner.

Spectroscopy. SNR is a critical aspect of understanding the uncertainties in spectral slope of a featureless visible–near-IR spectrum. In the case of 2023 DZ2, survey quality spectra from

Figure 10. Maps showing the likely damage swath due to the hypothetical impact of 2023 DZ2 for Epoch 1 (top panel) and Epoch 2 (bottom panel). In both panels, a subset of the possible results is shown along the impact corridor. For the subset of points, yellow represents a serious damage level, dark yellow represents a severe damage level, orange represents a critical damage level, and dark red represents an unsurvivable damage level.

GTC and the NASA IRTF did not show the weak 0.9 μm absorption feature due to the mineral pyroxene. As the object became brighter, higher-SNR data could be obtained that enabled the detection of this feature and helped confirm the affinity of 2023 DZ2 to aubrite meteorites. The experience gained from past campaigns helped us streamline the data reduction and analysis process for visible and near-IR spectral data.

Polarimetry. Polarimetric characterization can be used as a direct constraint on an asteroid's surface reflectivity properties (albedo). While there are other methods, such as thermal IR modeling, to constrain the albedo, each of these techniques have their own complications and specific restrictions on when these data can be obtained, so it is important that the community maintain a suite of capabilities to be able to rapidly respond to unknown targets, as was needed for the case of 2023 DZ2.

Thermal IR photometry. Smaller potentially hazardous asteroids (PHAs) such as 2023 DZ2 have narrow observing windows for characterization. For high-demand facilities like IRTF and techniques that require specific geometries like thermal infrared photometry and optical polarimetry, coordinating with scheduled observers to request interrupt time can take many days, and they are under no obligation to provide access. Standing observing allocations for interrupt time at

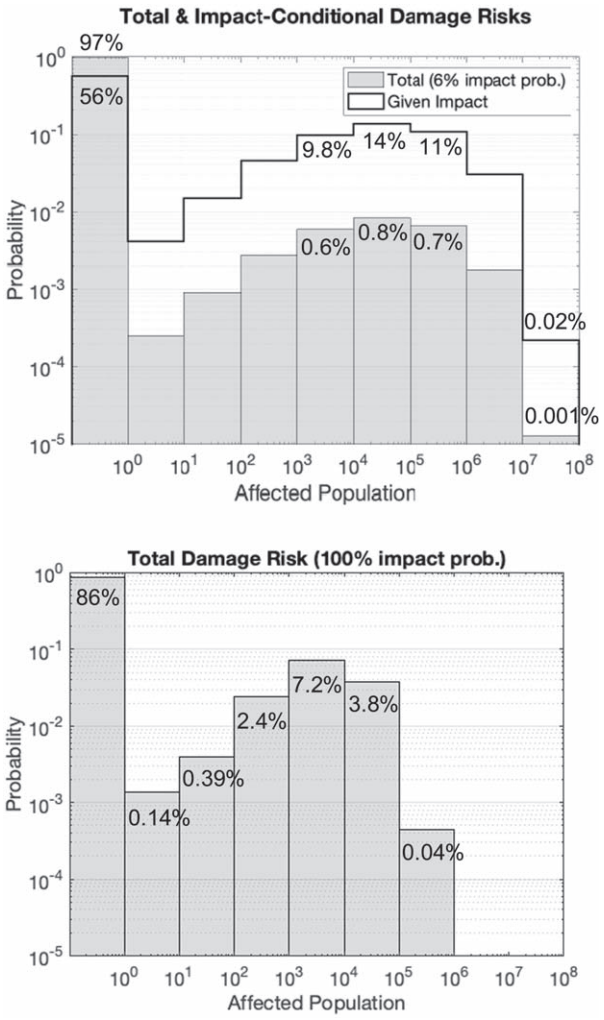

Figure 11. The affected population risks for Epoch 1 (top panel) and Epoch 2 (bottom panel). The most likely cause of damage remains the blast, but 86% of the cases result in no damage given the small diameter of 2023 DZ2.

facilities that are critical to planetary defense characterization will be important for future rapid response needs.

Radar. Radar observations were unusually challenging due to the very short round-trip light travel time and the time it takes during monostatic observations to switch between transmitting and receiving. Goldstone equipment and software take about 2 s to switch, but we seldom attempt monostatic observations of asteroids that are this close, and we had to modify software to make this work. The bistatic configuration simplifies observations for very close and/or slowly rotating objects, and it reduces the SNR.

In summary, the DZ2 campaign was extremely successful in demonstrating the global planetary defense community's ability to react to an incoming NEA on short notice. All characterization information was collected and processed in near-real time, and the community was able to discuss the results and pass them to the risk assessment team in a timely manner. The results from multiple techniques (photometric colors, spectroscopy, thermal IR modeling, polarimetry, radar) all converged to a single taxonomic type for 2023 DZ2, which is a testament to the robustness of NEO characterization techniques. This enabled us to run the PAIR model for two epochs within the short weeklong observing window for this campaign and produce meaningful results. The four planetary defense campaigns that we have undertaken so far have focused on NEAs, which make up much of the NEO population. The next planetary defense campaign could focus on comets, which make up a small fraction of the NEO population by numbers but still pose a credible hazard to the Earth.

Acknowledgments

The 2023 DZ2 campaign was conducted as part of the International Asteroid Warning Network (IAWN). IAWN is supported by the Planetary Data System (PDS) Small Bodies Node (SBN) at the University of Maryland College Park. Part of this research was conducted at the Jet Propulsion Laboratory, California Institute of Technology, and was performed under a contract with the National Aeronautics and Space Administration (NASA). This material is based in part on work supported by NASA under the Science Mission Directorate Research and Analysis Programs. This work has made use of data from the Asteroid Terrestrial-impact Last Alert System (ATLAS) project. The ATLAS project is primarily funded to search for near-Earth asteroids through NASA grants NN12AR55G, 80NSSC18K0284, and 80NSSC18K1575; by-products of the NEO search include images and catalogs from the survey area. This work was partially funded by Kepler/K2 grant J1944/80NSSC19K0112 and HST GO-15889 and STFC grants ST/T000198/1 and ST/S006109/1. The ATLAS science products have been made possible through the contributions of the University of Hawaii Institute for Astronomy, the Queen's University Belfast, the Space Telescope Science Institute, the South African Astronomical Observatory, and the Millennium Institute of Astrophysics (MAS), Chile. This work is partially supported by the South African National Research Foundation (NRF). Parts of this work were supported by the Russian Ministry of Science and Higher Education via the State Assignment Projects FEUZ-2023-0019 and FEUZ-2020-0038. TRAPPIST is a project funded by the Belgian Fonds (National) de la Recherche Scientifique (F.R.S.-FNRS) under grant PDR T.0120.21. TRAPPIST-North is a project funded by the University of Liège, in collaboration with the Cadi Ayyad University of Marrakech (Morocco). The 1.2 m Kryoneri telescope is operated by the Institute for Astronomy, Astrophysics, Space Applications and Remote Sensing of the National Observatory of Athens. T.S.R. acknowledges funding from the NEO-MAPP project (H2020-EU-2-1-6/870377). This work was partially supported by the Spanish MICIN/AEI/10.13039/501100011033 and by "ERDF A way of making Europe"' by the European Union through grant PID2021-122842OB-C21 and the Institute of Cosmos Sciences University of Barcelona (ICCUB, Unidad de Excelencia "María de Maeztu") through grant CEX2019-000918-M. The work by P.P. and his team at Ondrejov on observations with the Danish 1.54 m telescope at La Silla were supported by the Grant Agency of the Czech Republic, grant 23-04946S. We thank the NASA IRTF staff for making possible the last-minute schedule of MIRSI's observations for this international campaign. Also, we thank Cristina Thomas for giving us part of the observing block for the MITHNEOS program. The work at NASA Ames was supported by NASA's Planetary Defense Coordination Office. Supercomputing resources supporting this work were provided by the NASA High-End Computing (HEC) Program through the NASA Advanced Supercomputing (NAS) Division at NASA Ames Research Center. T.S.R. acknowledges funding from Ministerio de Ciencia e Innovación (Spanish Government), PGC2021, PID2021-125883NB-C21. This work was (partially) supported

by the Spanish MICIN/AEI/10.13039/501100011033 and by "ERDF A way of making Europe" by the European Union through grant PID2021-122842OB-C21, and the Institute of Cosmos Sciences University of Barcelona (ICCUB, Unidad de Excelencia"María de Maeztu") through grant CEX2019-000918-M. The Joan Oró Telescope (TJO) of the Montsec Observatory (OdM) is owned by the Catalan Government and operated by the Institute for Space Studies of Catalonia (IEEC).

ORCID iDs

Vishnu Reddy https://orcid.org/0000-0002-7743-3491
Jessie Dotson https://orcid.org/0000-0003-4206-5649
Nicolas Erasmus https://orcid.org/0000-0002-9986-3898
Davide Farnocchia https://orcid.org/0000-0003-0774-884X
Tyler Linder https://orcid.org/0000-0003-2534-673X
Joseph R. Masiero https://orcid.org/0000-0003-2638-720X
Cristina Thomas https://orcid.org/0000-0003-3091-5757
James Bauer https://orcid.org/0000-0001-9542-0953
Miguel R. Alarcon https://orcid.org/0000-0002-8134-2592
Daniel Bamberger https://orcid.org/0000-0002-9138-2942
Adam Battle https://orcid.org/0000-0002-4412-5732
Zouhair Benkhaldoun https://orcid.org/0000-0001-6285-9847
David C. Cantillo https://orcid.org/0000-0001-6018-1729
Sunil Chandra https://orcid.org/0000-0002-8776-1835
Francesca DeMeo https://orcid.org/0000-0002-8397-4219
Joseph L. Hora https://orcid.org/0000-0002-5599-4650
Kamil Hornoch https://orcid.org/0000-0002-0835-225X
Emmanuel Jehin https://orcid.org/0000-0001-8923-488X
Peter Kušnirák https://orcid.org/0000-0001-6098-6893
Julia de León https://orcid.org/0000-0002-0696-0411
Alexios Liakos https://orcid.org/0000-0002-0490-1469
Tim Lister https://orcid.org/0000-0002-3818-7769
Andy Lopez-Oquendo https://orcid.org/0000-0002-2601-6954
Shantanu P. Naidu https://orcid.org/0000-0003-4439-7014
Petr Pravec https://orcid.org/0000-0001-8434-9776
Juan Sanchez https://orcid.org/0000-0002-0764-4672
Miquel Serra-Ricart https://orcid.org/0000-0002-2394-0711
David E. Trilling https://orcid.org/0000-0003-4580-3790
Guy Wells https://orcid.org/0000-0002-6667-6535

References

Battle, A., Reddy, V., Sanchez, J. A., et al. 2022, PSJ, 3, 226
Beniyama, J., Sako, S., Ohtsuka, K., et al. 2023, ApJ, 955, 143
Belskaya, I., Cellino, A., Gil-Hutton, R., Muinonen, K., & Shkuratov, Y. 2015, in Asteroids IV, ed. P. Michel, F. E. DeMeo, & W. F. Bottke (Tucson, AZ: Univ. Arizona Press), 151
Bendjoya, Ph., Cellino, A., Rivet, J.-P., et al. 2022, A&A, 665, A66
Benner, L. A. M., Ostro, S. J., Giorgini, J. D., et al. 1997, Icar, 130, 296
Benner, L. A. M., Ostro, S. J., Magri, C., et al. 2008, Icar, 198, 294
Binzel 2000, P&SS, 48, 297
Binzel, R. P., DeMeo, F. E., Turtelboom, E. V., et al. 2019, Icar, 324, 41
Bowell, E., Hapke, B., Domingue, D., et al. 1989, Asteroids II (Tucson, AZ: Univ. Arizona Press), 524
Cellino, A., Bagnulo, S., Gil-Hutton, R., et al. 2015, MNRAS, 451, 3473
Chesley, S. R., Chodas, P. W., Milani, A., et al. 2002, Icar, 159, 423, Icar
Clark, B. E., Bus, S. J., Rivkin, A. S., et al. 2004, JGR, 109, E02001
Cushing, M. C., Vacca, W. D., & Rayner, J. T. 2004, PASP, 116, 362
Dandy, C. L., Fitzsimmons, A., & Collander-Brown, S. J. 2003, Icar, 163, 363
Delbo, M. 2006, NASA Planetary Data System, EAR-A-KECK1LWS/ETAL-5-DELBO-V1.0, https://pds.nasa.gov/ds-view/pds/viewProfile.jsp?dsid=EAR-A-KECK1LWS/ETAL-5-DELBO-V1.0
DeMeo, F. E., Binzel, R. P., Slivan, S. M., & Bus, S. J. 2009, Icar, 202, 160
DeMeo, F. E., & Carry, B. 2013, Icar, 226, 723
Devogele, M., Cellino, A., Bagnulo, S., et al. 2017, MNRAS, 465, 4335
Devogele, M., Cellino, A., Borisov, G., et al. 2018, MNRAS, 479, 3498
Dymock, R. 2007, JBAA, 117, 342
Erasmus, N., Mcneill, A., & Mommert, M. 2018, ApJS, 237, 19
Farnocchia, & Chodas 2021, RNAAS, 5, 257
Harris, A. W. 1998, Icar, 131, 291
Janse van Rensburg, P. 2021, MS thesis, Univ. Cape Town
Lebofsky, L. A., & Spencer, J. R. 1989, in Asteroids II, ed. R. P. Binzel, T. Gehrels, & M. S. Matthews (Tucson, AZ: Univ. Arizona Press), 128
Lomb, N. R. 1976, Ap&SS, 39, 447
Lord, S. D. 1992, NASA Technical Memorandum 103957
Mainzer, A. K., Bauer, J. M., Cutri, R. M., et al. 2019, NEOWISE Diameters and Albedos V2.0, urn:nasa:pds:neowise_diameters_albedos::2.0 NASA Planetary Data System
Mainzer, A., Bauer, J., Cutri, R. M., et al. 2014, ApJ, 792, 30
Mainzer, A., Grav, T., Bauer, J., et al. 2011, ApJ, 743, 156
Mathias, D. L., Wheeler, L. F., & Dotson, J. L. 2017, Icar, 289, 106
Ostro, S. J. 1993, RvMP, 65, 1235
Pernechele, C., Abe, L., Bendjoya, P., et al. 2012, Proc. SPIE, 8446, 84462H
Popescu, M. M., Văduvescu, O., de León, J., et al. 2023, A&A, 676, A126
Popova, O., Borovicka, J., Hartmann, W. K., et al. 2011, M&PS, 46, 1525
Rayner, J. T., Toomey, D. W., Onaka, P. M., et al. 2003, PASP, 115, 362
Reddy, V., Kelley, M. S., Farnocchia, D., et al. 2019, Icar, 326, 133
Reddy, V., Kelley, M. S., Dotson, J., et al. 2022a, Icar, 374, 114790
Reddy, V., Kelley, M. S., Dotson, J., et al. 2022b, PSJ, 3, 123
Rumpf, C. M., Lewis, H. G., & Atkinson, P. M. 2017, GeoRL, 44, 3433
Sanchez, J. A., Michelsen, R., Reddy, V., & Nathues, A. 2013, Icar, 225, 131
Sanchez, J. A., Reddy, V., Dykhuis, M., Lindsay, S., & Le Corre, L. 2015, APJ, 808, 93
Scargle, J. D. 1982, ApJ, 263, 835
Shevchenko, V. G., Krugly, Yu. N., Chiorny, V. G., Belskaya, I. N., & Gaftonyuk, N. M. 2003, P&SS, 51, 525
Stokes, G. H., Barbee, B. W., Bottke, W. F., et al. 2017, Report of the Near-Earth Object Science Definition Team
Trilling, D. E., Mueller, M., Hora, J. L., et al. 2010, AJ, 140, 770
Virkki, A. K., Marshall, S. E., Venditti, F. C. F., et al. 2022, PSJ, 3, 222
Virtanen, P., Gommers, R., Oliphant, T. E., et al. 2020, NatMe, 17, 261
Wheeler, L. F., Register, P. J., & Mathias, D. L. 2017, Icar, 295, 149
Zellner, B. 1979, in Asteroids, ed. T. Gehrels & M. S. Matthews (Tucson, AZ: Univ. Arizona Press), 783